



# Deformation behavior of a Co-Cr-Fe-Ni-Mo medium-entropy alloy at extremely low temperatures

Jongun Moon<sup>1</sup>, Elena Tabachnikova<sup>2</sup>, Sergii Shumilin<sup>2</sup>, Tetiana Hryhorova<sup>2</sup>, Yuri Estrin<sup>3,4</sup>, Jamieson Brechtl<sup>5</sup>, Peter K. Liaw<sup>6</sup>, Wenqing Wang<sup>7</sup>, Karin A. Dahmen<sup>7</sup>, Alireza Zargaran<sup>8</sup>, Jae Wung Bae<sup>9</sup>, Hyeon-Seok Do<sup>1</sup>, Byeong-Joo Lee<sup>1</sup>, Hyoung Seop Kim<sup>1,8,10</sup>,\*

We report the mechanical and microstructural characteristics of a medium-entropy alloy,  $Co_{17.5}Cr_{12.5}$ - $Fe_{55}Ni_{10}Mo_5$  (atomic percent, at%) at cryogenic temperatures, down to a record low temperature of 0.5 K. The alloy exhibits excellent strength and ductility combined with a high strain-hardening rate in the entire temperature range investigated. Its property profile, including the yield strength, ultimate tensile strength, strain hardening capability, and absorbed mechanical energy, is better than those of most alloys and HEAs used in cryogenics. Within the interval of extremely low temperatures considered (0.5–4.2 K), the alloy exhibits several unusual features, including anomalies of the temperature dependence of the yield strength and tensile ductility, discontinuous plastic deformation (DPF), and a change in the propensity for the deformation-induced martensitic transformation. While the occurrence of these effects in the same temperature interval may be fortuitous, we hypothesize that they are interrelated and provide a tentative explanation of the observed phenomena on this basis.

Keywords: Medium-entropy alloy; Cryogenic temperatures; Discontinuous plastic deformation; Martensitic phase transformation; Dislocation

#### Introduction

Over the past two decades, a new class of high- and mediumentropy alloys (HEAs and MEAs) has been developed, and research in this area is burgeoning [1–9]. The definition of HEAs/MEAs is generally specified in terms of the configurational entropy ( $\Delta S_{conf}$ ) of the alloys as follows [10]:

$$1.5R \le \Delta S_{conf}(\text{HEAs}) \tag{1}$$

$$1.0R \le \Delta S_{conf} < 1.5R(\text{MEAs}) \tag{2}$$

where R is the gas constant. Among these materials, face-centered-cubic (FCC) HEAs/MEAs exhibit exceptional mechanical

<sup>&</sup>lt;sup>1</sup> Department of Materials Science and Engineering, Pohang University of Science and Technology (POSTECH), Pohang 37673, Republic of Korea

<sup>&</sup>lt;sup>2</sup> B. Verkin Institute for Low Temperature Physics and Engineering of National Academy of Sciences of Ukraine, Kharkov 61103, Ukraine

<sup>&</sup>lt;sup>3</sup> Department of Materials Science and Engineering, Monash University, Clayton, VIC 3800, Australia

<sup>&</sup>lt;sup>4</sup> Department of Mechanical Engineering, The University of Western Australia, Crawley, WA 6009, Australia

<sup>&</sup>lt;sup>5</sup> The Bredesen Center for Interdisciplinary Research and Graduate Education, The University of Tennessee, Knoxville, TN 37996, USA

<sup>&</sup>lt;sup>6</sup> Department of Materials Science and Engineering, The University of Tennessee, Knoxville, TN 37996, USA

<sup>&</sup>lt;sup>7</sup> Department of Physics, University of Illinois at Urbana-Champaign, 1110 West Green Street, Urbana, IL 61801, USA

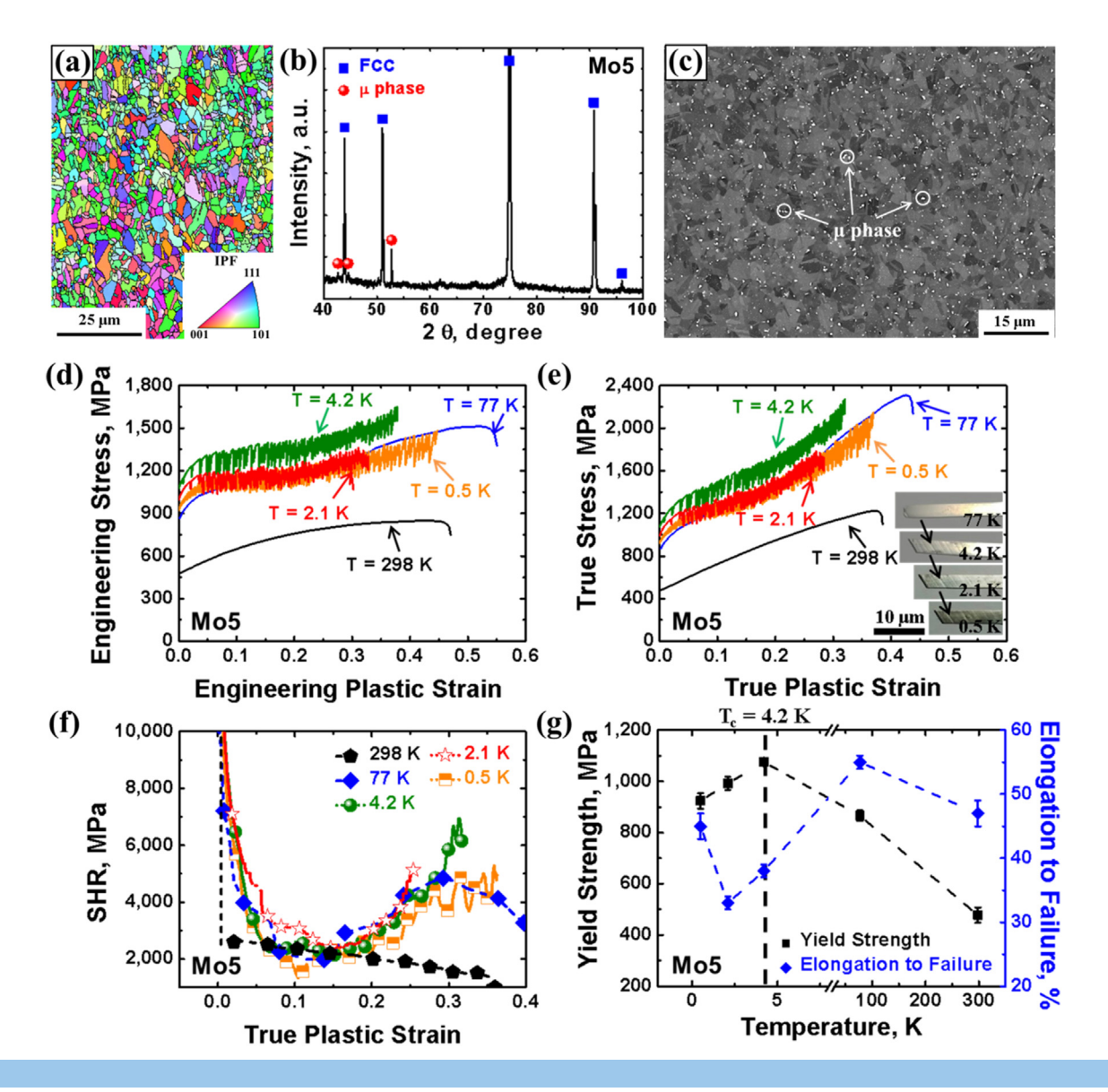
<sup>&</sup>lt;sup>8</sup> Graduate Institute of Ferrous Technology, Pohang University of Science and Technology (POSTECH), Pohang 37673, Republic of Korea

<sup>&</sup>lt;sup>9</sup> Max-Planck-Institut für Eisenforschung, Max-Planck-Straße 1, 40237 Düsseldorf, Germany

<sup>&</sup>lt;sup>10</sup> Center for High Entropy Alloys, Pohang University of Science and Technology (POSTECH), Pohang 37673, Republic of Korea

<sup>\*</sup> Corresponding author.

E-mail address: Kim, H.S. (hskim@postech.ac.kr)



Initial microstructure and low-temperature mechanical properties of the Mo5 alloy. (a) Electron backscatter diffraction (EBSD) IPF map, (b) XRD pattern, and (c) SEM-BSE image of the annealed Mo5 alloy. The white particles in (c) are identified as  $\mu$  precipitates. (d) Engineering and (e) true stress–strain curves for the Mo5 alloy at different temperatures. Photographs of fractured tensile samples deformed at different temperatures are inserted in (e). (f) Variation of the strain-hardening rate (SHR) with strain during the low-temperature tensile deformation. (g) Temperature dependence of the yield strength and the elongation to failure (as a measure of ductility) of the alloy exhibiting anomalies below a critical temperature set notionally at 4.2 K.

properties at cryogenic temperatures owing to strengthening by stacking faults [2], deformation-induced twinning [3,7], and/or deformation-induced martensitic transformation (DIMT) [4,5]. In particular, the 'metastability engineering' approach to DIMT, whereby phase stability is controlled through the chemical composition and deformation temperature, has been widely used in design of new HEAs/MEAs [4,5]. Recently, metastable ferrous MEAs possessing excellent strain hardening and tensile strength characteristics at 77 K were developed [5]. These properties are believed to be a result of DIMT from the FCC to body-centered-cubic (BCC) crystal structure [5].

The interest in the mechanical response of HEAs/MEAs at even lower temperatures is driven by their potential use in struc-

tures designed for outer-space applications. Note that the average temperature of the outer space associated with the cosmic microwave background is 2.725 K [11]. Here, we report a study of the mechanical properties and the deformation-induced microstructure evolution of the dual-phase MEA  $\rm Co_{17.5}Cr_{12.5}Fe_{55}Ni_{10}Mo_5$  (atomic percent, at %, Mo5) in a broad temperature range from room temperature down to 0.5 K. This is a first report on the mechanical response of a two-phase HEA/MEA at this record low temperature, which complements the scarce data for 'single-phase' HEAs [12] and MEAs [13] at 0.5 K. Several specific low-temperature effects, including a discontinuous plastic flow (DPF) and an anomalous temperature dependence of the flow stress and ductility, encountered as one moves down the Kelvin

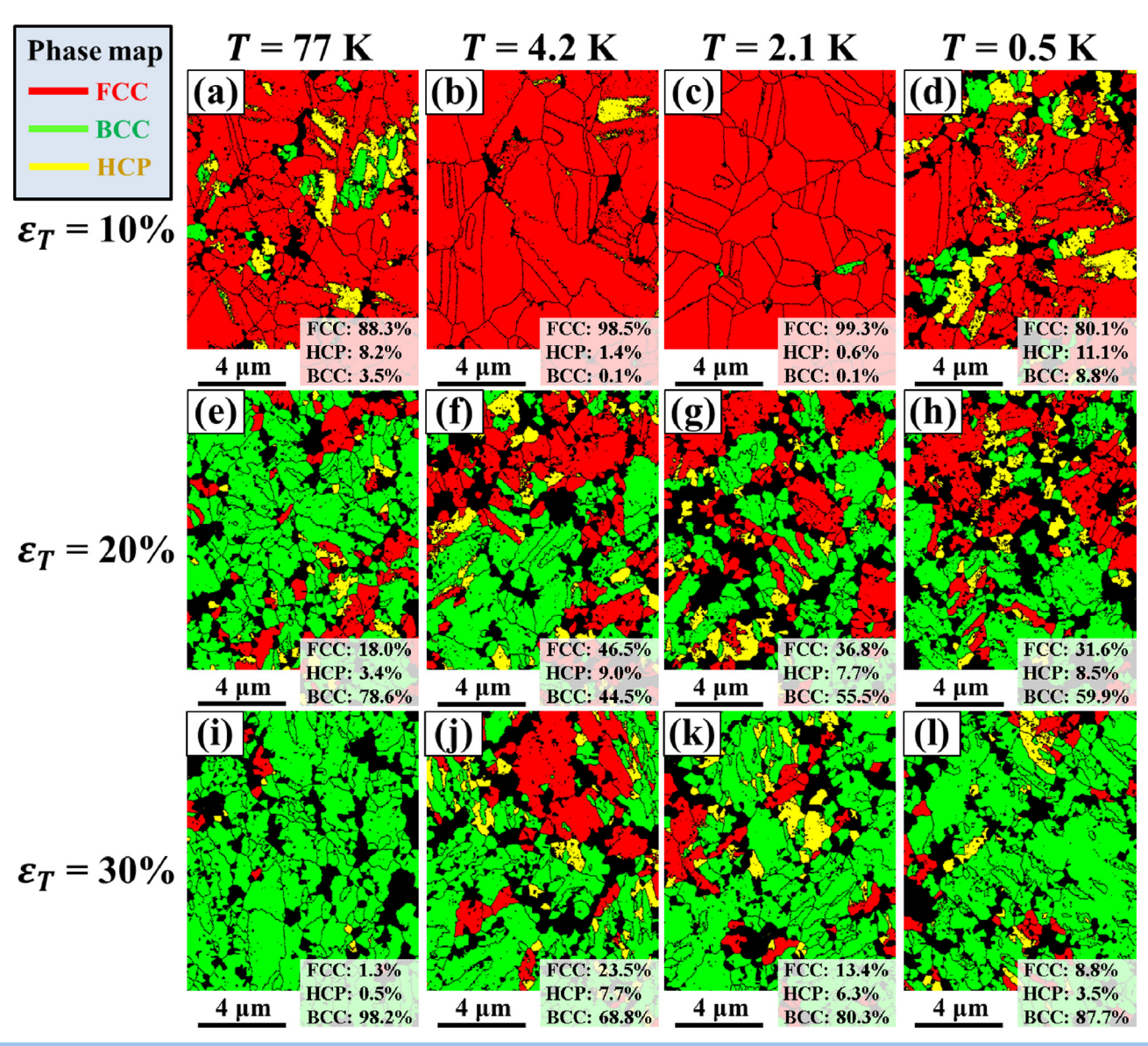


FIGURE 2

EBSD phase maps of the Mo5 alloy deformed in the low-temperature range. The EBSD-phase map for the Mo5 alloy after tensile deformation to a  $\varepsilon_T$  of (a–d) 10%, (e–h) 20%, and (i–l) 30% at various temperatures: (a, e, and i) 77 K, (b, f, and j) 4.2 K, (c, g, and k) 2.1 K, and (d, h, and l) 0.5 K. The insets in (a–l) indicate the fractions of the FCC, HCP, and BCC phases.

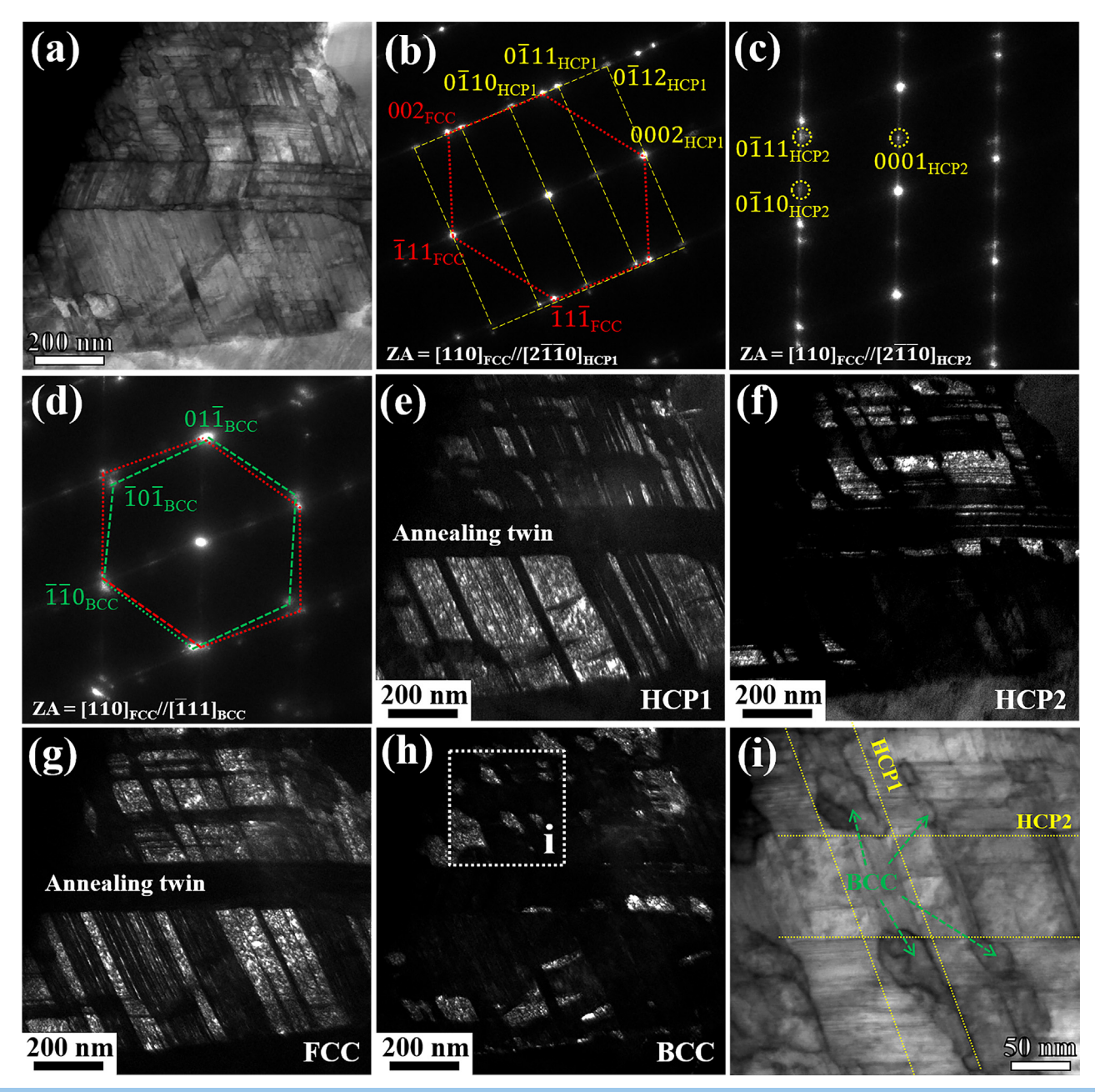
temperature scale, will be described. While earlier reports dealt with the superior mechanical properties of Ni-based superalloys [14] and HEAs/MEAs [2–5,7,15–18] at liquid nitrogen temperature (77 K), the unusual features of the microstructural evolution and the mechanical response of a dual-phase Mo5 MEA at the liquid helium temperature (4.2 K) and below have not been reported so far. The technical challenges of such testing are formidable. They stem from the need to employ pumping out liquid <sup>3</sup>He vapors to utilize its relatively high refrigerating capacity, compared to liquid <sup>4</sup>He at temperatures below 1 K. This difficulty is compounded by the requirement to minimize the heat release from the sample during deformation and the heat transfer through the grips of the testing machine for the stabilization of the experiment temperature. The data provided, especially those for the extremely low-temperature part of this interval,

down to 0.5 K, are unique in the HEA/MEA context. We shall also hypothesize on the mechanisms responsible for these phenomena observed in this extreme range of deformation temperatures.

#### Results

## Initial microstructure and mechanical properties

The initial microstructure of the annealed Mo5 alloy is presented in Fig. 1. The inverse pole figure (IPF) map shows that the annealed alloy is fully recrystallized, and the grains are randomly oriented (Fig. 1a). The average grain size of the annealed alloy is  $3.82 \pm 1.82~\mu m$ . The X-ray diffraction (XRD) pattern reveals that the annealed alloy comprises an FCC matrix with  $\mu$  precipitates (Fig. 1b) [6]. The scanning electron microscope-backscattered



TEM images of the Mo5 alloy deformed at 4.2 K. (a) Bright-field TEM image of the alloy after tensile deformation to a  $\varepsilon_T$  of 30% at 4.2 K. The corresponding SAD patterns of (b) HCP1, (c) HCP2, and (d) BCC phases are presented with respect to the FCC [1 1 0] zone axis. The two HCP variants observed are referred to as HCP1 and HCP2. The dark-field TEM images correspond to phases identified as (e) HCP1, (f) HCP2, (g) FCC, and (h) BCC. (i) Bright-field TEM image of the corresponding region of (h) showing BCC phases formed at the intersections of HCP phases.

electron (SEM-BSE) image in Fig. 1c also shows the occurrence of fine  $\mu$  precipitates dispersed in the matrix. The average size and the areal fraction of the  $\mu$  precipitates are 354.32  $\pm$  125.06 nm and 3.21  $\pm$  0.26%, respectively.

Fig. 1d and e present the engineering and true stress–strain curves of the Mo5 alloy at different temperatures. The alloy exhibits an excellent level of the flow stress at 77 K and below (Fig. 1d and e), while retaining ductility, as represented by the elongation to failure. Mo5 obviously owns its good ductility to the high strain-hardening rate (SHR) that it possesses in the extremely

low temperature range, which is on par with the room-temperature SHR, Fig. 1f. As the temperature decreases down to 4.2 K, the yield strength and the tensile strength of the alloy rise significantly, which represents the behavior typical of thermally activated plastic deformation [19]. In particular, at 4.2 K, the material exhibits a remarkably high peak yield strength of 1,075 MPa and the highest tensile strength of 1,651 MPa. The high yield strength of Mo5 is attributed to multiple strengthening mechanisms, including solid-solution, precipitation, and grain-boundary hardening, as well as a contribution from a high

dislocation density [6]. The observed trend is reversed between 4.2 K and 2.1 K when the yield strength starts to drop as the temperature is lowered (Fig. 1g), which indicates a yield strength anomaly. A critical temperature  $(T_c)$  for the yield-strength anomaly of the Mo5 alloy can be set notionally at 4.2 K (although the strength may actually attain a peak value at a somewhat different temperature close to 4.2 K). The temperature dependence of the elongation to failure of the alloy shows a complex behavior: upon lowering the temperature, the elongation to failure increases between 298 K and 77 K, drops between 77 K and 2.1 K, and then increases again between 2.1 K and 0.5 K (Fig. 1g). The temperature interval of 2.1–4.2 K is most problematic, as both the yield strength and the elongation to failure of the alloy drop when the temperature is reduced from 4.2 K to 2.1 K (Fig. 1g). It should be emphasized, however, that this relative loss of strength and ductility is moderate, and both characteristics can still be considered as remarkably good. A fact to be noted is that the character of the deformation, which is continuous at 77 K and upwards, becomes discontinuous at and below 4.2 K. This observation suggests that the temperature anomaly of the flow stress, also seen in the same temperature range, and DPF may be interrelated. At T<sub>c</sub> and below, localized shear bands (LSBs), about 50 µm in width, were observed on the surface of the deformed tensile samples, as illustrated in the inset in Fig. 1e. Along with the pronounced serrations on the stressstrain curves, the occurrence of LSBs can be regarded as a footprint of plastic instability at extremely low temperatures.

# Deformed microstructures and underlying deformation mechanisms

Fig. 2 shows the microstructures of the Mo5 alloy formed during tensile deformation at various test temperatures. The EBSD phase maps for Mo5 deformed at cryogenic temperatures reveal that a DIMT from FCC to hexagonal close-packed (HCP) and BCC phases occurs. This transformation of the initial FCC phase to HCP and BCC phases sets in at a true strain ( $\varepsilon_T$ ) of 10% (Fig. 2a–d). With further straining, profuse BCC DIMT proceeds, and the fraction of the BCC phase increases substantially, while that of the HCP phase stays below 10% during low-temperature

deformation (Fig. 2e–l). The large values of the tensile strength and the SHR of the Mo5 alloy (Fig. 1d–f) are attributed to the DIMT and the attendant hindering of dislocation mobility by martensite particles during the low-temperature deformation.

Transmission electron microscopy (TEM) images of the alloy deformed at 4.2 K are shown in Fig. 3. In Fig. 3a, band-like structures are observed in the FCC matrix. These formations are HCP phases occurring in two variants, as revealed by the selected area diffraction (SAD) patterns (Fig. 3b, c, e, f, and g). Deformationinduced BCC phases are also found at the intersections of the HCP phases (Fig. 3d, h, and i). It should be noted that the intersections of deformation twins, HCP martensite particles, and shear bands serve as nucleation sites for the BCC martensite [5]. Neither deformation-induced twins nor stacking faults were detected in the samples deformed at 0.5 K-4.2 K. Notably, the formation of the HCP phase stems from overlapping stacking faults on every second {1 1 1} plane [20]. However, stacking faults other than those leading to the formation of the HCP phase were not observed in the present work. Similarly, the microstructures of the alloy deformed at 2.1 K and 0.5 K show the occurrence of the DIMT from FCC to HCP and BCC phases (Figs. S1 and S2).

Fig. 4a presents the areal fraction of the BCC phase after tensile deformation at various testing temperatures. It is seen that at 77 K, DIMT of FCC to BCC phases is almost complete at  $\varepsilon_T$  = 30%, with the corresponding BCC-phase fraction amounting to 98.2% (Fig. 4a). Interestingly, the areal fraction of the BCC phase at a strain of 30% dropped to 68.8% when the alloy was deformed at 4.2 K, and then rose to 80.3% and 87.7%, as the testing temperature was further reduced to 2.1 K and 0.5 K, respectively (Fig. 4a). The trend observed at  $\varepsilon_T$  = 30% is the same at an intermediate value of strain,  $\varepsilon_T$  = 20%, as well. This 'phase-transformation anomaly' takes place between 77 K and 4.2 K.

The evolution of the dislocation density in the Mo5 alloy, as measured by the XRD line-profile analysis, is presented in Fig. 4b. The initial dislocation density prior to deformation was  $1.71 \times 10^{14}$  m<sup>-2</sup>. With increasing  $\varepsilon_T$ , the dislocation density rose significantly, attaining an order of magnitude of  $\sim 10^{16}$  m<sup>-2</sup>. Notably, the highest dislocation density was achieved in the specimens deformed at 4.2 K, followed by those deformed at

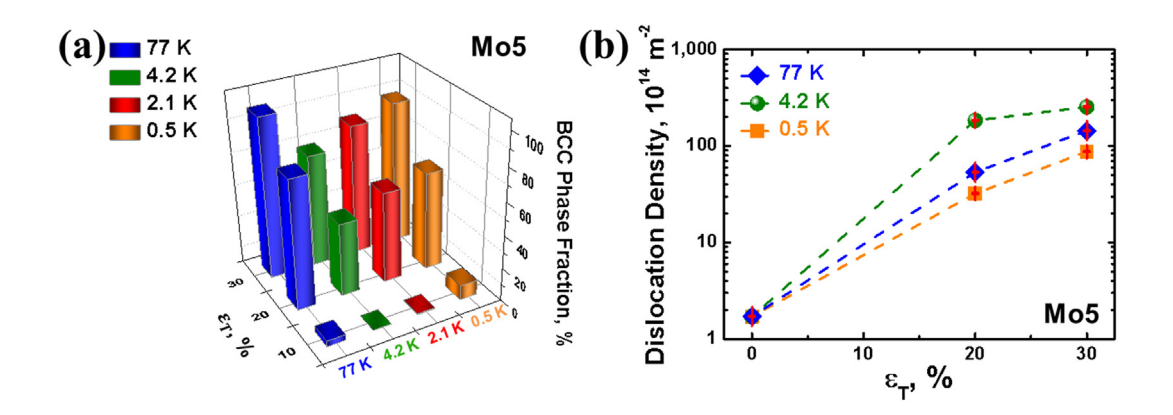


#### FIGURE 4

Variations in the BCC phase fraction and the dislocation density with the true strain,  $\varepsilon_T$ , and temperature. (a) Temperature dependence of the phase fraction of the BCC phase for various levels of the true strain,  $\varepsilon_T$ . (b) Dislocation density evolution in the FCC phase with  $\varepsilon_T$  at different temperatures. The red lines in (b) indicate the error bars showing that the precision of the dislocation density data is better than 15%.

77 K and 0.5 K. The dislocation density evolution exhibited a nonmonotonic trend in the temperature interval between 4.2 K and 77 K where the phase-transformation anomaly occurred.

#### Fractography

Fig. 5 displays SEM images of the fracture surfaces of the Mo5 alloy deformed at cryogenic temperatures. The fracture mode of the alloy deformed at 77 K presents a typical ductile fracture with dimples (Fig. 5a). However, the fracture surface of the alloy deformed at 4.2 K is divided into two regions (Fig. 5b): one which has dimples (Fig. 5c), while the other has a smooth appearance (Fig. 5d). Fig. 5d reveals that micro-voids are nucleated at the  $\mu$ -phase boundary within the matrix. In the alloy deformed at 2.1 K, the isolated dimple colonies appear on the smooth fracture surface (Fig. 5e). In addition, ductile dimples and singular cleavage facets are observed in the fractured alloy deformed at 0.5 K (Fig. 5f).

#### Discussion

#### Yield strength anomaly

Explaining all low-temperature phenomena reported above, *viz.* the yield strength and ductility anomalies, discontinuous deformation, anomaly of the DIMT, and nonmonotonic evolution of the dislocation density, is a challenging task. The yield strength anomaly is best explained by the inertial motion of dislocations below  $T_c$  [21,22]. In conventional FCC metals and alloys, the yielding and plastic flow are determined by the interaction of dislocations with local obstacles to their motion [23]. Overcoming the obstacles by moving dislocations is a thermally activated process, which is the case at sufficiently high deformation temperatures. This feature is the physical reason for the commonly observed temperature dependence of the yield stress, which increases as the temperature is reduced [19,24]. An inverse trend

may be associated with a lack of thermal activation [25]. Below a certain temperature, which was defined as  $T_c$ , viscous drag of dislocations during their motion between the localized obstacles becomes low, as its phonon component drops significantly [26]. Under these conditions, dislocations overcome the localized barriers by the inertial motion, without the assistance of thermal fluctuations, which results in a decrease in yield strength with lowering temperature.

#### Discontinuous plastic flow (DPF)

In Fig. 1g,  $T_c$  is also recognizable as a 'watershed' temperature separating the DPF and continuous plastic flow (CPF) regimes. The origin of DPF, as explained by several authors [27–30], lies in the thermomechanical coupling. As long as plastic deformation is controlled by the thermally activated dislocation motion, i.e., above  $T_c$ , the deformation-induced heat release accelerates the rate of the plastic flow. This trend, in turn, further boosts the heat generation. Under certain circumstances depending on the mechanical and thermal properties of the material and the deformation conditions, including the geometry of the specimen and heat exchange with the environment, this thermomechanical coupling leads to an instability of the plastic flow [30]. The instability is manifested in repeated load drops seen as serrations on the stress-strain curves. However, such a mechanism does not work below the critical temperature,  $T_c$ , where the inertial, rather than thermally activated, deformation mechanisms are prevalent. Under such conditions, discontinuous yielding may be caused by the following mechanism proposed in Refs. [23,27–31]. Below a certain temperature, which is materialdependent, the reduced mobility of screw dislocations originating from the insufficient thermal energy leads to the inhibition of cross-slip [27,28]. The scarcity of cross-slip causes the accumulation of dislocations at local barriers, and dislocations break

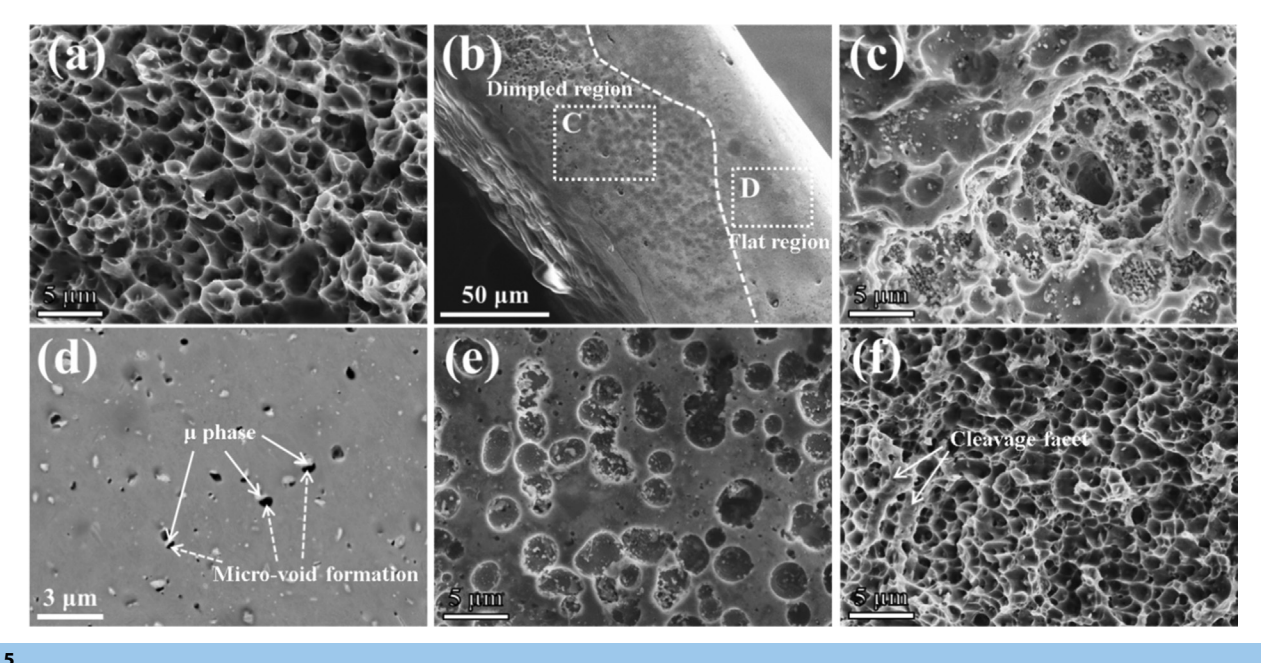


FIGURE 5

SEM images of the fracture surfaces of the Mo5 alloy deformed at 77 K-0.5 K. Fracture surfaces of the alloy deformed at (a) 77 K, (b-d) 4.2 K, (e) 2.1 K, and (f) 0.5 K. (c and d) represent the high-magnification images of the corresponding region of (b).

away from barriers in an avalanche-like fashion [23,27–31], which results in serrations on the stress–strain curves. The crucial role of the dislocation ability to cross-slip in serrated yielding of the CoCrFeMnNi alloy at very low temperatures (4.2–35 K) was emphasized in a recent publication by Tirunilai et al. [32]. A thermomechanical coupling-based mechanism was ruled out as a possible cause for plastic instability at extremely low temperatures, as was deformation-induced twinning or  $\epsilon$ -martensite formation.

Fig. 6 shows the analysis of the dislocation character of the Mo5 alloy deformed at 4.2 K by TEM two-beam imaging. The dislocation character is manifested in a mixture of edge, screw, and mixed components. However, edge dislocations are more abundant than screw dislocations. The measured dislocation densities of edge and screw components in the TEM images are 1.61  $\times$  $10^{14}~\text{m}^{-2}$  and  $5.82\times10^{13}~\text{m}^{-2}$ , respectively. This trend shows that the edge dislocations are predominant at 4.2 K. This feature may be associated with insufficiency of thermal energy for the movement of screw dislocations, and that may be seen as a cause of the observed DPF and low-temperature anomalies. It should also be noted that entangled dislocations were observed in the alloy deformed at 2.1 K and 0.5 K (Fig. S3). Dislocation entanglement is associated with cross-slip of dislocations [33], which supports the view that screw dislocations become more active during deformation at 2.1 K and 0.5 K. The unusual predominance of screw dislocations at such low temperatures will be discussed in the following section.

The HCP and BCC phases generated by DIMT are probable local obstacles hindering the dislocation movement. The DIMT

transforming the FCC to an HCP phase cannot contribute to DPF since no dislocation multiplication occurs in that case [34]. On the other hand, mobile dislocations can be pinned by BCC martensite particles [35]. Accordingly, pinning of dislocations at the transformed BCC phase may affect the DPF of the present alloy. Precipitates can be another kind of barriers to dislocation motion [36], causing strain localization that results in DPF. In our case, inspection of the fracture surfaces revealed the formation of micro-voids at the boundaries of  $\mu$ -phase precipitates (Fig. 5d), which is an indication of the occurrence of strain localization there.

# Phase-transformation anomaly and dislocation density evolution

To better understand a conjugated relationship between the DPF, the phase-transformation anomaly, and the dislocation density evolution and to quantify the adiabatic heating effect, thermodynamic calculations were performed. Fig. 7a shows the temperature dependence of the difference of the Gibbs free energies between BCC and FCC phases [ $\Delta G(BCC\text{-}FCC)$ ] of the Mo5 alloy. This quantity declines as the temperature is decreased, and below 862 K, the BCC phase becomes metastable. The intense DIMT at 77 K can be rationalized in terms of the strong temperature dependence of the calculated  $\Delta G(BCC\text{-}FCC)$ .

According to earlier works [27,28], the stored plastic strain energy arising from dislocation pile-ups is converted to heat during the stress drops accompanying DPF The heat exchange process is considered to occur under adiabatic conditions [27,28]. Indeed, the thermal conductivity approaches zero in

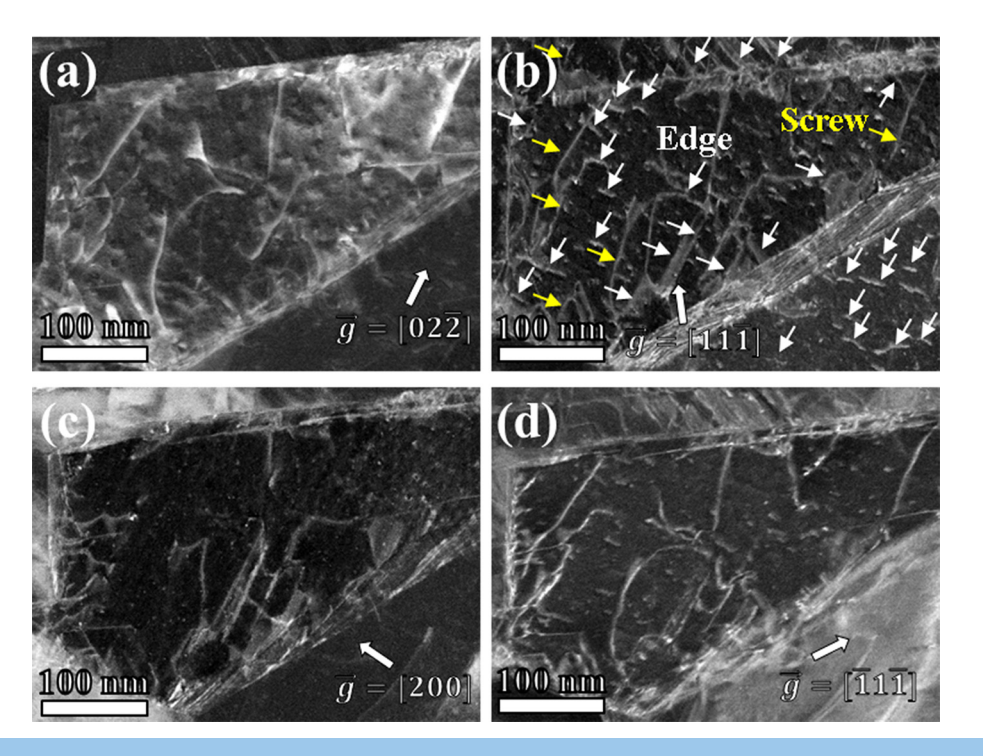
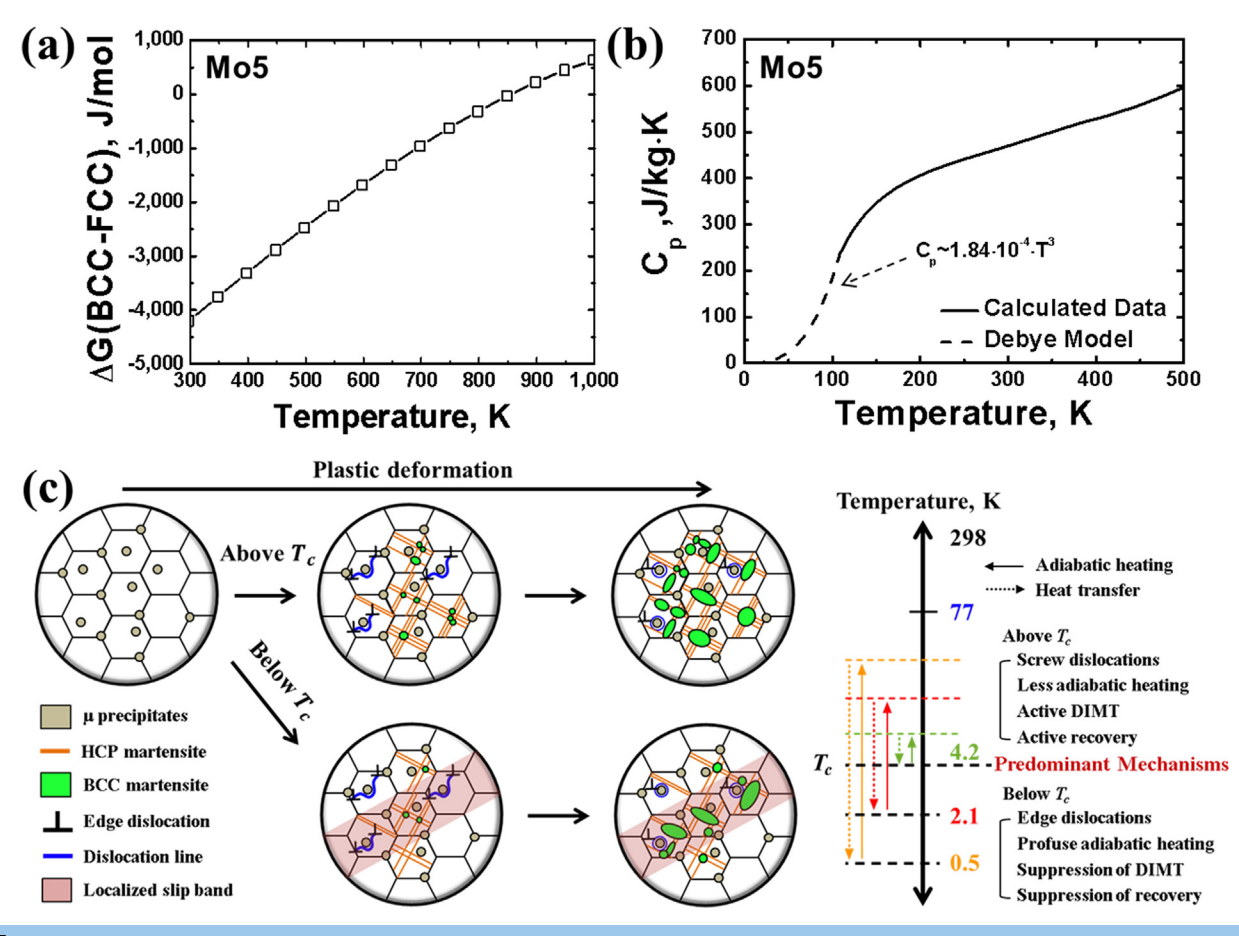


#### FIGURE 6

Analysis of the dislocation character for the Mo5 alloy deformed at 4.2 K by TEM two-beam imaging. The TEM two-beam images of the alloy after tensile deformation to a  $\varepsilon_T$  of 5% at 4.2 K with different diffraction vectors,  $\overrightarrow{g}$ : (a)  $\left[02\overline{2}\right]$ , (b)  $\left[11\overline{1}\right]$ , (c)  $\left[200\right]$ , and (d)  $\left[\overline{1}1\overline{1}\right]$  revealing the dislocation character. The white and yellow arrows in (b) indicate edge and screw components of dislocations, respectively. The edge and screw dislocations are identified by being in the visible and invisible states according to different  $\overrightarrow{g}$  under the two-beam condition.



Thermodynamic calculation results and predominant temperature-dependent mechanisms for the Mo5 alloy. Calculated temperature dependence of (a)  $\Delta G$  (BCC-FCC) and (b) specific heat capacity ( $C_p$ ) for the Mo5 alloy. (c) A schematic of the microstructure evolution and temperature-dependent processes pertinent to the observed low-temperature behavior. The solid and dotted arrows in (c) represent, respectively, the temperature rise or fall due to adiabatic heating and heat transfer. Each green, red, and orange arrow corresponds to the test temperature of 4.2, 2.1, and 0.5 K, respectively.

the extremely low temperature range of interest [27], which favors the conditions for adiabatic heating. The local temperature increment ( $\Delta T$ ) in the adiabatic condition, when the rate of the mechanical work is well in excess of the rate of heat removal to the thermal bath, can be expressed as follows [24]:

$$\Delta T = \frac{\beta}{\rho C_p} \int_{\varepsilon_s^p}^{\varepsilon_f^p} \sigma d\varepsilon^p \tag{3}$$

where  $\rho$  is the material's density (8.067 g·cm<sup>-3</sup> for Mo5),  $\sigma$  is the true flow stress,  $\varepsilon_s^p$  and  $\varepsilon_f^p$  denote the true plastic strains at the start and finish of a stress drop, respectively, and  $\beta$  is the efficiency factor for heat conversion, usually taken as 0.9 [24]. We note that in the adiabatic condition, the local temperature increment given by Eq. (3) grows with the plastic strain irrespective of the strain rate. The strain rate affects the local temperature increment only indirectly, through the strain rate dependence of the flow stress.

Fig. 7b displays the temperature dependence of  $C_p$  of the Mo5 alloy used in the following estimates. This quantity was calculated down to 100 K, which is below the Debye temperature  $(T_D)$  according to thermodynamic calculations. Below 100 K,  $C_p$  was estimated, using the Debye model [37], which predicts

that  $C_p$  is proportional to  $T^3$ . The Debye temperature,  $T_D$ , entering the model was obtained, using a known analytical equation [38] and a rule of mixtures for the parameters in this equation. The calculated value of  $T_D$  for the Mo5 alloy is ~365 K.

Using Eq. (3) and the estimated value for  $C_p$ , the calculated temperature increment,  $\Delta T$ , associated with a stress drop at the true plastic strain of 20% and the test temperature of 4.2 K is ~267 K. In reality, the local temperature rise may not be as high as this estimated value because the generated heat will be partially transferred to the cooling medium and the grips of the testing machine [27,28]. Nevertheless, the increase in the local temperature during the DPF can be considerable. It should be noted that  $C_p$  decreases further with a reduction in the test temperature. Accordingly, the temperature rise due to the adiabatic heating effect at the test temperatures of 2.1 K and 0.5 K will be higher than at 4.2 K.

A possible scenario accounting for the dislocation density evolution is the dynamic recovery process. Dynamic recovery is known to be governed by cross-slip and annihilation of screw dislocations [39]. This mechanism is inhibited at extremely low temperatures due to the paucity of screw dislocations. Conse-

quently, the dislocation density increases, reaching the highest levels at 4.2 K. At 0.5 K, by contrast, adiabatic heating facilitates dynamic recovery by cross-slip of screw dislocations, resulting in a lower dislocation density than at 4.2 K. This tendency is also reflected in the SHR curves (Fig. 1f), where the saturation of SHR occurs towards the end of deformation at 0.5 K.

Our tentative explanations for the anomalies in the phase transformation and dislocation density evolution in the deep cryogenic temperature range are illustrated in Fig. 7c. Above  $T_c$ , the DIMT from the FCC to BCC phase is favorable owing to a limited phase stability of the FCC structure. However, according to the previous studies [27,28], this transformation is inhibited below  $T_c$ . This trend is attributed to the mentioned transition from the predominantly screw character of mobile dislocations to the edge type below  $T_c$ . The motion of screw dislocations is essential for the DIMT because the junctions of intersecting screw dislocations act as nucleation sites for the BCC martensite [28]. On the other hand, the preferential motion of edge dislocations below  $T_c$  causes strain localization in LSBs under the adiabatic conditions. The adiabatic heat generation during DPF raises the local temperature to levels well above  $T_c$ . Thus, a considerable quantity of the BCC martensite can be generated during adiabatic heating [28]. As the test temperature is decreased, the extent of the local temperature rise becomes greater due to a reduction in  $C_p$ . Since heat transfer becomes more restricted as the test temperature is reduced, strain localization associated with adiabatic heating, and thus DIMT, becomes more pronounced. The deformed microstructures of the alloy inside and outside LSBs for  $\varepsilon_T$  = 30% at 4.2 K are shown in Figs. S4a and b. The volume fraction of the BCC phase inside the LSBs is 77.7%, whereas that outside the LSBs is 56.2%. Since the BCC volume fraction at the same applied  $\varepsilon_T$  determined at a greater magnification is 68.8% (Fig. 2j), it can be concluded that the DIMT is more active inside the LSBs. However, the scarcity of mobile screw dislocations comes into play when the temperature is lowered. An interplay of these two opposite effects is believed to be the reason for the phase-transformation anomaly observed in the temperature range between 77 K and 4.2 K.

#### Mechanical characteristics

The yield strength ( $\sigma_{YS}$ ) of the present alloy can be expressed as a linear superposition of the contributions from several mechanisms:

$$\sigma_{YS} = \sigma_0 + \Delta \sigma_{GB} + \Delta \sigma_D + \Delta \sigma_P \tag{4}$$

where  $\sigma_0$  is the lattice friction and the terms,  $\Delta \sigma_{GB}$ ,  $\Delta \sigma_P$ , and  $\Delta \sigma_D$ , are associated with grain-boundary strengthening, precipitate hardening, and strain hardening, respectively. The  $\Delta \sigma_{GB}$  term can be estimated using the Hall-Petch relation [40]:

$$\Delta \sigma_{GB} = k_{HP} d^{-1/2} \tag{5}$$

where  $k_{HP}$  is the Hall-Petch strengthening coefficient and d is the average grain size (3.82 µm). From the data in Ref. [6],  $k_{HP}$  for the present alloy can be estimated at 168 MPa·µm<sup>-1/2</sup>. Thus,  $\Delta\sigma_{GB}$  assumes the value of about 86 MPa. The strain-hardening term,  $\Delta\sigma_D$ , is related to the dislocation density through the Taylor equation [41]:

$$\Delta \sigma_D = M \alpha_D G b \rho_D^{1/2} \tag{6}$$

where M is the Taylor factor (3.06 for FCC metals [41]),  $\alpha_D$  is a constant (typically 0.2 [41]), G is the shear modulus (87.6 GPa for Mo5), b is the magnitude of the Burgers vector [0.255 nm for Mo5 (Fig. 1b)], and  $\rho_D$  is the dislocation density [1.71  $\times$  10<sup>14</sup> m<sup>-2</sup> in the annealed state (Fig. 4b)]. The shear modulus, G, is determined by a rule of mixtures involving the constituent elements of the alloy [42,43]. The maximum strain hardening contribution,  $\Delta\sigma_D$ , can be estimated, using Eq. (6), to be  $\sim$  178 MPa.

The term, $\Delta \sigma_P$ , stemming from the  $\mu$  precipitates can be associated with the Orowan stress [44]. Indeed, the hard  $\mu$  precipitates in the present alloy cannot be sheared by gliding dislocations [6] and are overcome by the Orowan mechanism, whose schematics are shown in Fig. 7c. This mechanism gives rise to a stress:

$$\Delta \sigma_P = M \frac{0.4Gb}{\pi \lambda} \frac{\ln(2\bar{r}/b)}{\sqrt{1-\nu}} \tag{7}$$

where  $\lambda$  is the edge-to-edge spacing between precipitates given by:

$$\lambda = 2\bar{r}(\sqrt{\frac{\pi}{4f}} - 1) \tag{8}$$

and  $\bar{r}$  is the mean radius of a circular cross-section in a random plane for a spherical precipitate:

$$\bar{r} = r\sqrt{2/3} \tag{9}$$

Here r is the mean radius estimated at 177 nm (Fig. 1c). Other quantities in Eq. (7) are Poisson's ratio, v (set at 0.3), and the volume fraction, f, of the precipitate phase [3.21% (Fig. 1c)]. The summation of  $\Delta\sigma_{GB}$ ,  $\Delta\sigma_{D}$ , and  $\Delta\sigma_{P}$  gives the estimated overall strength of the alloy, which amounts to 380 MPa. The yield strength of Mo5 is 478 MPa (Fig. 1g). Therefore, the lattice friction term,  $\sigma_{0}$ , can be estimated to be ~98 MPa, which is in the same ball park as the friction stress for other FCC-based HEAs (125 MPa for CoCrFeMnNi [45] and 134 MPa for  $V_{10}Cr_{15}Mn_{5}Fe_{35}Co_{10}Ni_{25}$  [46]).

The increased ductility of the alloy between 298 K and 77 K (Fig. 1g), which is reflected by a greater elongation to failure within this temperature range, can be explained by strain hardening that results from DIMT. According to the previous studies [4,5], it is established that the 'transformation-induced plasticity (TRIP)' effect can enhance both strength and ductility. It is therefore not surprising that at 77 K, the alloy exhibits ductile fracture (Fig. 5a). However, below  $T_c$ , the DIMT is suppressed, and strain localization occurs. It should be noted that the fracture surfaces of the alloy deformed at 4.2 K and 2.1 K contain smooth regions (Fig. 5d and e). Smooth fracture surfaces are frequently observed in materials that deform by localized shear banding, such as bulk metallic glasses [47] or metals and alloys deformed by dynamic loading [48]. In the Mo5 alloy deformed at 4.2 K, two separated regions, one with dimples and the other with a smooth surface, demonstrate that the deformation is strongly localized. The occurrence of a dimpled region indicates a certain level of ductility. Once the deformation is localized at the  $\mu$  precipitates at 4.2 K, brittle cleavage-like debonding occurs along the LSBs. This trend results in a smooth fracture surface and poor elongation to failure. However, the picture is different at 2.1 K where dimpled

regions are observed over the entire fracture surface (Fig. 5e). The dimples are separated from each other and tend to form isolated colonies. Notably, Mo-enriched µ phases were found inside each individual dimple (Fig. S5). The adiabatic heating during the DPF at 2.1 K can facilitate cross-slip and DIMT, alleviating strain localization. Therefore, homogeneously distributed micro-voids can form and grow during the adiabatic heating. As the adiabatic heat dissipates to the cooling medium, the strain localization occurs with an inhibition of cross-slip and DIMT, which occurs repetitively during the DPF. This recurrent process isolates the micro-voids and dimples at 2.1 K. The insufficient coalescence of micro-voids and dimples leads to brittle fracture, and it causes an earlier failure of the alloy at 2.1 K than at 4.2 K (ductility anomaly). We note that at 0.5 K, cross-slip and DIMT are more profuse than at 4.2 K and 2.1 K, and occur due to a higher temperature rise during adiabatic heating. It is interesting to note that the TRIP effect enhances the elongation to failure of the alloy, and ductile fracture is observed at both ends of the lowtemperature interval, at 0.5 K and 77 K, as reflected in dimpled fracture surfaces for these temperatures (Fig. 5a and f).

The remarkable yield and tensile strengths, 1,075 MPa and 1,651 MPa, respectively, are achieved in the Mo5 alloy at 4.2 K. Because of the phase-transformation anomaly, the DIMT is less likely to occur at 4.2 K (Fig. 4a). However, due to the lack of dynamic recovery, the dislocation density at 4.2 K grows to a much higher level, compared to other temperature ranges (Fig. 4b). Furthermore, it is well known that the thermal stress component may stem from short-range obstacles to dislocation motion, such as the Peierls-Nabarro barriers and forest dislocation junctions [49]. Notably, the Peierls-Nabarro barriers serve as a type of obstacles in the thermally activated dislocation glide in BCC metals and alloys, and BCC alloys show a stronger temperature dependence of the thermal stress component than FCC alloys [49]. Thus, the BCC phase formed by DIMT in the present work may increase the lattice friction stress during deformation in the temperature range of 0.5 K-77 K. It may also lead to the strain partitioning and the generation of the back stress against FCC/BCC phase boundaries during deformation [5], which, in turn, enhances the strain hardening of the Mo5 alloy.

Let us now summarize the mechanical characteristics of alloy Mo5 at the liquid-helium temperature and compare them with the corresponding properties of other HEAs and MEAs as well as conventional FCC metals and alloys. Fig. 8a-i show the Ashby plots for the Mo5 alloy, Cu alloys [50,51], Al alloys [52], Ti alloys [53–55], 9% (weight percent, wt%) Ni steels [56,57], stainless steels [55,58-61], and reported HEAs [3,62] and MEAs [7,63] for cryogenic applications. Fig. 8a and b display the yield strength  $(\sigma_{YS})$  and the tensile strength  $(\sigma_{TS})$  versus elongation to failure  $(\varepsilon_f)$  at room temperature (298 K). The product of  $\sigma_{TS}$  and  $\varepsilon_f$  $(\sigma_{TS} \times \varepsilon_f)$  that characterizes the absorbed mechanical work and is related to the toughness is plotted versus  $\sigma_{TS}$  in Fig. 8c. These plots demonstrate that at room temperature, alloy Mo5 possesses an excellent combination of strength, ductility, and toughness. It is noteworthy that  $\sigma_{TS}$  and  $\sigma_{TS} \times \varepsilon_f$  of alloys Mo5 and CoCrNi exceed 750 MPa and 30,000 MPa·%, respectively (Fig. 8c). Even if the temperature is lowered to 77 K (Fig. 8d-f) and 4.2 K

(Fig. 8g–i), the Mo5 alloy overcomes the strength-ductility trade-off known for other conventional alloys and HEAs/MEAs, and its tensile properties are similar to those of stainless steels. The magnitude of  $\sigma_{TS} \times \varepsilon_f$  for Mo5 exceeds 60,000 MPa·% at 77 K and 4.2 K, which is remarkably high (Fig. 8f–i). Only a few stainless steels, which possess  $\sigma_{TS}$  above 1,500 MPa at 77 K and 4.2 K, can compete with the present Mo5 alloy with regard to tensile strength. Quite generally, it can be asserted that the Mo5 alloy outperforms most conventional alloys for cryogenic applications in terms of the overall property profile.

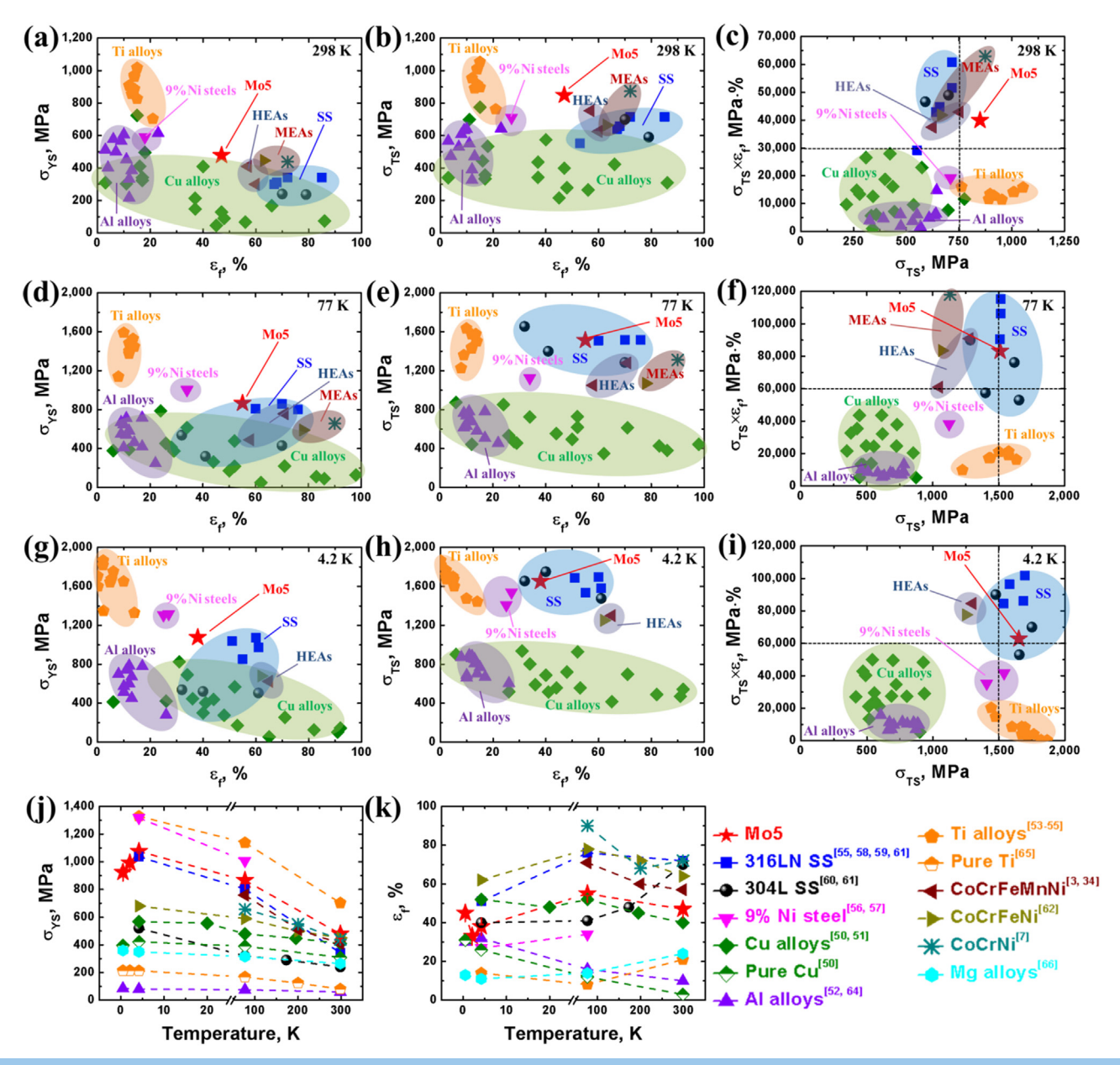
Fig. 8j and k show the temperature dependence of the quantities,  $\sigma_{YS}$  and  $\varepsilon_f$ , for the Mo5 alloy, conventional alloys [50,51,55,60,61,63–66], and HEAs [3,7,63] in the temperature range of 4.2 K-298 K. In all alloys being compared, an increase of  $\sigma_{YS}$  with decreasing temperature was observed. Notably, the Mo5 alloy exhibits a stronger temperature dependence of  $\sigma_{YS}$  than pure Cu [50], Cu-6Al-1.5Fe (wt%) [51], Al-3.9 Mg (wt%) [64], pure Ti [65], AZ31 [66], 316LN [55], 304L [60], CoCrNi [7], and CoCr-FeNi [63]. A deficiency in cross-slip and the presence of strong barriers to dislocation glide (such as μ precipitates) are the factors responsible for a strong temperature dependence of  $\sigma_{YS}$  of the alloy at deep cryogenic temperatures. Although the increased  $\sigma_{YS}$  of the Mo5 alloy at 4.2 K and above may be associated with the thermally activated dislocation motion [19], it is most probably the inertial mechanism that governs the motion of dislocations at temperatures below 4.2 K [21,22]. This is in keeping with the observation that below 4.2 K,  $\sigma_{YS}$  of pure Cu, Mg alloy AZ31, and Al-3.9 Mg (wt%) decreases with decreasing temperature or remains nearly constant, which is attributed to the inertial mechanism presumably operating there [23].

With regard to tensile ductility, the following conclusions can be drawn from the results presented here and in the literature. When the temperature decreases to 77 K, the elongation to failure,  $\varepsilon_f$ , increases for Mo5 (Fig. 1g), as it does for Cu alloys, 316LN SS, CoCrNi, CoCrFeNi, and CoCrFeMnNi. This increase was rationalized in terms of the deformation twinning [3,7,50,63] and the DIMT [31,58] mechanisms. An anomaly in the temperature dependence of ductility below 4.2 K was observed only in the present Mo5 alloy, and at this stage, it can only be speculated that it was caused by the peculiarities of the DPF and their effect on fracture (Fig. 5).

#### **Conclusions**

In summary, the mechanical properties and microstructural evolution of the Mo5 alloy were investigated systematically for very low deformation temperatures, including the deep cryogenic range down to 0.5 K. The unusual features reported in the current work, including the peculiar trend of the martensite fraction and the nonmonotonic evolution of dislocation density, were elucidated on the basis of the conjecture that the material undergoes thermomechanical coupling at the temperatures investigated. The following conclusions can be drawn:

• The medium-entropy alloy, Mo5, shows excellent mechanical properties at liquid nitrogen and liquid helium temperatures. Its property profile in terms of the yield strength, the ultimate



Mechanical characteristics of the Mo5 alloy, vis-à-vis those of other HEAs and MEAs (compiled from literature), as well as conventional FCC alloys. Ashby maps for (a-c) 298 K, (d-f) 77 K, and (g-i) 4.2 K plotting (a, d, and g) yield strength,  $\sigma_{YS}$  vs. elongation to failure,  $\varepsilon_f$ , (b, e, and h) tensile strength,  $\sigma_{TS}$  vs.  $\varepsilon_f$ , and (c, f, and i)  $\sigma_{TS} \times \varepsilon_f$  vs.  $\sigma_{TS}$ . Temperature dependence of (j)  $\sigma_{YS}$  and (k)  $\varepsilon_f$  in the temperature range of 0.5 K–298 K. SS stands for stainless steels.

tensile strength, the strain hardening capability, and the absorbed mechanical energy is better than those of most alloys and HEAs used in cryogenics.

- Owing to the deformation-induced martensitic transformation from FCC to BCC or, to a lesser extent, HCP crystal structures, the alloy Mo5 possesses excellent low-temperature mechanical properties, including a high yield strength (1,075 MPa) combined with a substantial strain hardening capability, leading to a tensile strength as high as 1,651 MPa at 4.2 K.
- For the first time ever, the mechanical properties of a dualphase MEA were studied at a record low temperature of 0.5 K. The properties of the alloy at this temperature were shown to be at least on par with those at the liquid helium temperature.
- Four characteristic phenomena, *viz.* discontinuous plastic deformation, temperature anomalies of the yield strength and ductility, and an anomaly in the temperature dependence of the deformation-induced martensitic transformation were found to occur in the temperature range from 4.2 K

downwards. We believe that the interrelation of these effects falling in roughly the same temperature range is not fortuitous. We conjecture that they are governed by common physical mechanisms.

- We hypothesize that the yield-strength anomaly and the discontinuous plastic flow are a result of the inertial mechanism of dislocation motion. The effect of the local temperature rise on the deformation-induced martensitic transformation and the dislocation density evolution in Mo5 were elucidated by considering the deformation-induced adiabatic heating. The temperature increment associated with the stress drops in the DPF regime changes the difference of the Gibbs free energies between the competing FCC and BCC phases. Consequently, it is the change in the preponderant type of dislocations from the screw to the edge one (in the temperature range of 0.5–4.2 K) that inhibits the capability of the material to undergo dynamic recovery via dislocation crossslip.
- The ductility anomaly was explained in terms of the fracture mechanism. Strain localization at 4.2 K and 2.1 K leads to catastrophic failure by fracture along localized shear bands, producing fracture surfaces with a large proportion of smooth areas. More ductile behavior at 77 K and 0.5 K is associated with the deformation-induced martensitic transformation, which effectively relieves strain localization and gives rise to greater elongation to failure with dimpled fracture surfaces.

#### Materials and methods

# Fabrication of the Co<sub>17.5</sub>Cr<sub>12.5</sub>Fe<sub>55</sub>Ni<sub>10</sub>Mo<sub>5</sub> alloy

An ingot of  $Co_{17.5}Cr_{12.5}Fe_{55}Ni_{10}Mo_5$  (atomic percent, at%) was fabricated, using vacuum induction melting (MC100V, Indutherm, Germany) in the high-purity argon inside a graphite mold. The purity of the alloying elements was above 99.9 weight percent (wt%). A rectangular ingot with dimensions of  $100 \times 35 \times 8 \text{ mm}^3$  was homogenized at 1,250 °C for 6 h in an argon atmosphere and milled to a thickness of 7 mm. Cold-rolling was carried out on the milled ingot with the thickness reduction from 7 mm to 0.6 mm, and then annealed at 900 °C for 1 h, followed by water quenching.

#### Tensile testing

Dog-bone shaped tensile samples with a gauge length of 15 mm and a width of 3 mm were fabricated for tensile testing. The surfaces of the annealed tensile samples were mechanically polished up to 1,200 SiC grit paper. Tensile testing was conducted at a strain rate of 10<sup>-4</sup> s<sup>-1</sup> at five different temperatures: 298 K, 77 K, 4.2 K, 2.1 K, and 0.5 K. The tensile tests were conducted in triplicate to ensure reproducibility of results. A sketch of the cryostat for cryogenic tensile testing is shown in Fig. S6. The temperature was measured with a semiconductor thermometer, which was placed near the tensile sample. A temperature of 77 K was obtained by placing the sample in liquid nitrogen; a temperature of 4.2 K was achieved by cooling in liquid helium-4 (4He). Finally, the temperatures of 2.1 K and 0.5 K were obtained by lowering the pressure above boiling liquids, <sup>4</sup>He and helium-3 (<sup>3</sup>He), respectively, through additional pumping out. The accuracy of temperature measurements was sustained within 4  $\times$  10<sup>-4</sup> K in <sup>4</sup>He and 2  $\times$  10<sup>-2</sup> K in <sup>3</sup>He, respectively. The method for obtaining these extremely low temperatures is described in detail in Ref. [67]."

#### Microstructure characterization

Scanning electron microscopy (SEM) with electron backscatter diffraction (EBSD), backscattered electron (BSE), and energy-dispersive spectroscopy (EDS) analyses were performed, using an FEI Helios 650 device. For EBSD, the TSL/OIM software [68] with a step size of 100 nm was employed. The deformed samples for SEM characterization were taken from the region of uniform elongation. The samples were polished, using 600, 800, and 1200 SiC grit papers and then electro-polished in an etchant solution of mixed 92% CH<sub>3</sub>COOH and 8 % HClO<sub>4</sub> (volume percent) to remove the scratches and the strain layer caused by mechanical polishing.

The transmission electron microscopy (TEM) and transmission Kikuchi diffraction (TKD) measurements were performed, employing a JEOL JEM-2100F microscope operating at an acceleration voltage of 200 kV and Bruker ESPRIT 2.1 software [69] with a step size of 15 nm. Specimens for TEM and TKD experiments were taken from tensile samples that underwent deformation up to true strains of 10% and 30% with a strain rate of  $10^{-4}$  s $^{-1}$  at 4.2 K, 2.1 K, and 0.5 K. They were milled from 1  $\mu m$  to a final thickness of 50 nm by employing a focused ion beam instrument (FEI, Helios 600) operated at 5 kV and 3° incidence of the Ga $^+$  ion beam.

The X-ray diffraction (XRD) measurements were performed, using a Rigaku D/MAX-2,500 device. For the XRD measurements, the surface of the annealed alloy was polished with 1200 SiC grit paper and then electropolished in the same fashion as the SEM samples. The XRD scans with the incident beam of Cu K $\alpha$  radiation (wavelength = 1.5418 Å) were conducted in the 2 $\theta$  range from 40° to 100° with a step size of 0.02° and a scan speed of 2°/min.

Synchrotron XRD measurements were conducted on the high-resolution powder diffraction beamline (9B) of the Pohang Light Source in Pohang, Korea. The X-ray radiation was monochromatized to the wavelength of 0.1522 nm by a Si (1 1 1) double-crystal monochromator. The synchrotron XRD scans were performed with a step size of 0.02° and a holding time of 10 s. Line-profile analysis of the obtained synchrotron XRD data to measure dislocation densities of the annealed and deformed specimens was performed, employing the convolutional multiple whole profile (CMWP) program [70].

#### Density measurement

The density of the present alloy was measured, using a Mettler Toledo analytical balance with deionized water.

#### Thermodynamic calculations

The Gibbs free energy and the specific heat capacity of the present alloy were calculated, employing the Thermo-Calc software [71] with a thermodynamic database, TCFE2000, and its upgraded version [72]. The temperature-dependent molar Gibbs free energy  $(G_m)$  for the face-centered-cubic (FCC) or body-centered-cubic (BCC) phases was calculated based on the following formula:

$$G_m = \sum_{i=C_O,Cr,Fe,Ni,Mo} x_i G_i + RT \sum_{i=C_O,Cr,Fe,Ni,Mo} x_i ln x_i + G_{m,ex} + G_{m,mag}$$
(1)

where  $x_i$  is the mole fraction of the respective element,  $G_i$  is its molar Gibbs free energy, R is the gas constant, and T is the absolute temperature. The excess Gibbs free energy  $(G_{m,ex})$  can be expressed by the Redlich-Kister polynomials [73]:

$$G_{m,ex} = \sum_{i=Co,Cr,Fe,Ni,Mo} x_i x_j L_{i,j} + \sum_{i=Co,Cr,Fe,Ni,Mo} x_i x_j x_k L_{i,j,k}; i \neq j \neq k$$
(2)

$$L_{i,j} = \sum_{i < i, p = 0} L_{i,j}{}^{p} (x_i - x_j)^{p}$$
(3)

$$L_{ij,k} = L_{i,i,k}^{0}(x_i + \delta_{i,j,k}) + L_{i,i,k}^{1}(x_i + \delta_{i,j,k}) + L_{i,i,k}^{2}(x_i + \delta_{i,j,k})$$
(4

where  $\partial_{i,j,k} = \frac{\left(1 - x_i - x_j - x_k\right)}{3}$ , and  $L_{i,j}$  and  $L_{i,j,k}$  are the interaction parameters for the i-j binary and i-j-k ternary systems, respectively. The magnetic Gibbs free energy ( $G_{m,mag}$ ) was determined by the Hillert-Jarl-Inden model [74].

The molar heat capacity  $(C_m)$  of the alloy was calculated as follows [75]:

$$C_m = -T \left( \frac{\partial^2 G_m}{\partial T^2} \right) \tag{5}$$

The specific heat capacity,  $C_p$ , of the Mo5 alloy was determined as the product of the  $C_m$  and molar mass of the alloy (0.0579 kg/mol). The molar mass of the alloy was estimated using a rule of mixtures for the alloying elements [76].

#### **CRediT authorship contribution statement**

Jongun Moon: Conceptualization, Data curation, Formal analysis, Investigation, Visualization, Writing - original draft. Elena Tabachnikova: Conceptualization, Data curation, Formal analysis, Validation, Writing - review & editing. Sergii Shumilin: Formal analysis, Investigation, Validation. Tetiana Hryhorova: Formal analysis, Investigation, Validation. Yuri Estrin: Formal analysis, Validation, Writing - review & editing. Jamieson Brechtl: Methodology, Formal analysis. Peter K. Liaw: Methodology, Formal analysis, Validation, Writing review & editing. Wenqing Wang: Methodology, Formal analysis. Karin A. Dahmen: Methodology, Formal analysis. Alireza Zargaran: Investigation, Formal analysis. Jae Wung Bae: Investigation, Formal analysis. Hyeon-Seok Do: Methodology, Formal analysis. Byeong-Joo Lee: Methodology, Formal analysis. Hyoung Seop Kim: Conceptualization, Validation, Resources, Supervision, Project administration, Funding acquisition, Writing - review & editing.

# **Declaration of Competing Interest**

The authors declare that they have no known competing financial interests or personal relationships that could have appeared to influence the work reported in this paper.

#### Acknowledgments

We are most grateful to the Editor and Reviewers for their excellent comments. The present work was supported by the Korea-Ukraine Bilateral Program through the National Research Foundation of Korea (NRF) funded by the Ministry of Science and Information and Communication Technology (ICT) [NRF-

2018K1A3A1A13087775]. The research was also supported by (1) the Future Materials Discovery Program through the NRF funded by the Ministry of Science and ICT [NRF-2016M3D1A1023384], and (2) the NRF grant funded by the Korea government (MSIP) [NRF-2021R1A2C3006662]. P. K. L. acknowledges the support from (1) the U.S. Army Office Project [W911NF-13-1-0438 and W911NF-19-2-0049] with the program managers, Drs. Michael P. Bakas, David M. Stepp, and S. Mathaudhu, and (2) the National Science Foundation [DMR-1611180 and 1809640] with the program directors, Drs. Judith Yang, Gary Shiflet, and Diana Farkas.

#### Appendix A. Supplementary data

Supplementary data to this article can be found online at https://doi.org/10.1016/j.mattod.2021.08.001.

#### References

- [1] B. Cantor et al., Mater. Sci. Eng. A 375-377 (2004) 213-218.
- [2] Y. Tong et al., Acta Mater. 165 (2019) 228-240.
- [3] B. Gludovatz et al., Science 345 (6201) (2014) 1153-1158.
- [4] Z. Li et al., Nature 534 (7606) (2016) 227-230.
- [5] J.W. Bae et al., Acta Mater. 161 (2018) 388-399.
- [6] J.W. Bae et al., J. Alloys Compd. 781 (2019) 75-83.
- [7] B. Gludovatz et al., Nat. Commun. 7 (2016) 10602.
- [8] J. Brechtl et al., Metals 10 (2020) 1101.
- [9] J.-W. Yeh et al., Adv. Eng. Mater. 6 (2004) 299-303.
- [10] I.-W. Yeh. IOM 65 (12) (2013) 1759–1771.
- [11] https://wmap.gsfc.nasa.gov/universe/bb\_cosmo\_fluct.html..
- [12] E.D. Tabachnikova et al., Low Temp. Phys. 43 (9) (2017) 1108-1118.
- [13] T.V. Hryhorova et al., J. V. N. Karazin Kharkiv Natl. Univ., Phys. 32 (2020) 41–48
- [14] Q. Ding et al., Mater. Today Nano 14 (2021) 100110.
- [15] W. Zhao et al., Met. Mater. Int. (2020), https://doi.org/10.1007/s12540-020-00869-5. in press.
- [16] Y. Kim et al., Met. Mater. Int. 27 (7) (2021) 2300–2309.
- [17] J. Lee et al., Met. Mater. Int. 27 (1) (2021) 166–174.
- [18] D. Li et al., Acta Mater. 123 (2017) 285–294.
- [19] V.L. Indenbom, Y.Z. Estrin, Phys. Status Solidi A 4 (1) (1971) K37–K39.
- [20] J. Talonen, H. Hänninen, Acta Mater. 55 (18) (2007) 6108-6118.
- [21] Y.Z. Estrin, Sov. J. Low-Temp. Phys. 1 (1975) 45.
- [22] E.Y. Gutmanas, Y. Estrin, Phys. Status Solidi A 92 (1) (1985) 137-147.
- [23] V.V. Pustovalov, Low Temp. Phys. 26 (6) (2000) 375–390.
- [24] J.M. Park et al., Mater. Sci. Eng. A 719 (2018) 155-163.
- [25] M.S. Colla et al., Nat. Commun. 6 (2015) 5922.
- [26] V. I. Alshits, V. I. Indenbom, Mechanisms of dislocations drag, in: F. R. N. Nabarro, (Eds.), Dislocations in solids, Elsevier Science Pub. Co., North-Holland, Amsterdam, 1986, Vol. 7, pp. 43-111..
- [27] B. Skoczeń et al., Int. J. Plast. 26 (12) (2010) 1659-1679.
- [28] B. Obst, A. Nyilas, Mater. Sci. Eng. A 137 (1991) 141–150.
- [29] M.A. Laktionova, E.D. Tabachnikova, Low Temp. Phys. 39 (2013) 630–632.
- [30] Y. Estrin, L.P. Kubin, Scripta Metall. 14 (12) (1980) 1359–1364.
- [31] X. Guo et al., Phys. Lett. 111 (2017) 251905.
- [32] A.S. Tirunilai et al., Acta Mater. 200 (2020) 980–991.
- [33] D. Jang et al., Nat. Nanotechnol. 7 (9) (2012) 594–601.
- [34] M. Koyama, T. Sawaguchi, K. Tsuzaki, Philos. Mag. 92 (2012) 3051–3063.
- [35] B. Sun et al., Scripta Mater. 133 (2017) 9-13.
- [36] E.D. Tabachnikova et al., J. Alloys Compd. 698 (2017) 501–509.
- [37] Z. Zhou, C. Uher, App. Phys. Lett. 89 (2006) 031924.
- [38] D. Ma et al., Acta Mater. 100 (2015) 90-97.
- [39] M. Zehetbauer, V. Seumer, Acta Metall. Mater. 41 (2) (1993) 577–588.
- [40] E.O. Hall, Proc. Phys. Soc. B 64 (9) (1951) 747–753.
- [41] J.M. Park et al., Mater. Res Lett. 8 (1) (2020) 1-7.
- [42] K. Edalati, Z. Horita, Acta Mater. 59 (2011) 6831–6836.
- [43] K. Edalati et al., Acta Mater. 69 (2014) 68-77.
- [44] H. Wen et al., Acta Mater. 61 (8) (2013) 2769-2782.
- [45] F. Otto et al., Acta Mater. 61 (15) (2013) 5743–5755.[46] P. Asghari-Rad et al., Mater. Sci. Eng. A 744 (2019) 610–617.
- [47] G.N. Yang, Y. Shao, K.F. Yao, Sci. Rep. 6 (2016) 21852.

- [48] S.Y. Wu et al., Mater. Charact. 137 (2018) 58-66.
- [49] M.A. Meyers, Dynamic Behavior of Materials, John Wiley & Sons Inc., New York, 1994, pp. 337–345.
- [50] Y. Estrin et al., Acta Mater. 54 (20) (2006) 5581-5590.
- [51] http://www.copper.org/resources/properties/144\_8/..
- [52] R.P. Reed et al., Aluminum alloys for ALS cryogenic tanks: Comparative measurements of cryogenic mechanical properties of Al-Li alloys and alloy 2219, Tech. Rep. PB-93-173441/XAB; NISTIR-3979, National Inst. of Standards and Technology, USA, 1993..
- [53] K. Nagai et al., ISIJ Int. 31 (8) (1991) 882-889.
- [54] M. Reytier, F. Kircher, B. Levesy, AIP Conf. Proc. 614 (2002) 76-83.
- [55] T. Ogata, K. Nagai, K. Ishikawa, Adv. Cryo. Eng. Mater. 40 (1994) 1191-1198.
- [56] C.K. Syn, S. Jin, J.W. Morris, Metall. Trans. A 7 (11) (1976) 1827–1832.
- [57] N. Nakada et al., Mater. Sci. Eng. A 374 (1-2) (2004) 137-144.
- [58] W. Han et al., J. Nucl. Mater. 504 (2018) 29-32.
- [59] H. Zhang et al., Cryogenics 106 (2020) 103058.
- [60] H. Yoshimura, T. Shimizu, K. Kitajima, Trans. ISIJ 22 (1982) 577-585.
- [61] B.T. Skoczeń, Compensation Systems for Low Temperature Applications, Springer Berlin Heidelberg, Berlin, Heidelberg, 2004.

- [62] M. Naeem et al., Sci. Adv. 6 (13) (2020) eaax4002.
- [63] J. Liu et al., Sci. China Mater. 62 (2019) 853-863.
- [64] S.E. Shumilin et al., Adv. Eng. Mater. 14 (1-2) (2012) 35-38.
- [65] V.A. Moskalenko, V.D. Natsik, V.N. Kovaleva, Low Temp. Phys. 31 (10) (2005) 907–914.
- [66] S.E. Shumilin et al., Adv. Eng. Mater. 15 (5) (2013) 352–357.
- [67] I.N. Kuzmenko, V.V. Pustovalov, Cryogenics 25 (6) (1985) 346–351.
- [68] TexSEM Lab (TSL), OIM Data Collection software version 7..
- [69] Bruker, Espirit Microanalysis software version 2.2..
- [70] G. Ribárik, J. Gubicza, T. Ungár, Mater. Sci. Eng. A 387-389 (2004) 343-347.
- [71] B. Sundman, B. Jansson, J.O. Andersson, Calphad 9 (2) (1985) 153–190.
- [72] TCFE2000: The Thermo-Calc Steels Database, upgraded by B. J. Lee & B. Sundman at KTH, KTH Royal Institute of Technology, Stockholm, 1999..
- [73] O. Redlich, A.T. Kister, Ind. Eng. Chem. 40 (2) (1948) 345-348.
- [74] M. Hillert, M. Jarl, Calphad 2 (1978) 227-238.
- [75] C.V. Thompson, F. Spaepen, Acta Metall. 27 (12) (1979) 1855–1859.
- [76] M.E. Wieser, T.B. Coplen, Pure Appl. Chem. 83 (2011) 359–396.